

PAPER

Multi-resonant metamaterials based on self-sensing piezoelectric patches and digital circuits for broadband isolation of elastic wave transmission

To cite this article: Kaijun Yi *et al* 2022 *Smart Mater. Struct.* **31** 015042

View the [article online](#) for updates and enhancements.

You may also like

- [Metamaterials at the University of Southampton and beyond](#)
Nikolay I Zheludev
- [Roadmap on optical metamaterials](#)
Augustine M Urbas, Zubin Jacob, Luca Dal Negro *et al.*
- [Perspective of additive manufacturing for metamaterials development](#)
Xin Wu, Yutai Su and Jing Shi



The Electrochemical Society
Advancing solid state & electrochemical science & technology

242nd ECS Meeting

Oct 9 – 13, 2022 • Atlanta, GA, US

Abstract submission deadline: **April 8, 2022**

Connect. Engage. Champion. Empower. Accelerate.

MOVE SCIENCE FORWARD



Submit your abstract



Multi-resonant metamaterials based on self-sensing piezoelectric patches and digital circuits for broadband isolation of elastic wave transmission

Kaijun Yi* , Zhiyuan Liu  and Rui Zhu

School of Aerospace Engineering, Beijing Institute of Technology, Beijing 100081, People's Republic of China

E-mail: kaijun.yi@bit.edu.cn

Received 11 August 2021, revised 1 November 2021

Accepted for publication 18 November 2021

Published 10 December 2021



Abstract

This paper proposes a general method to design multi-resonant piezoelectric metamaterials. Such metamaterials contain periodically distributed piezoelectric patches bonded on the surfaces of a host structure. The patches are shunted with digital circuits and working on self-sensing mode. A transfer function to be implemented in the digital circuits is designed to realize multi-resonance. The transfer function is derived only using the parameters of the patches. Consequently, it can be used to realize any type of multi-resonant metamaterial structures, like beams, plates and shells. The mechanism of generating multi-bandgaps by the transfer function is explained by analytically studying the effective bending stiffness of a multi-resonant piezo-metamaterial plate. It is shown that the transfer function induces multiple frequency ranges in which the effective bending stiffness becomes negative, consequently results in multiple bandgaps. The characteristics of these bandgaps are investigated, coupling and merging phenomena between them are observed and analyzed. Isolation effects of vibration transmission (elastic wave) in the metamaterials at multiple line frequencies or within a broad frequency band are numerically verified in frequency domain. Further time domain simulations accounting for the full dynamics of the metamaterials with digital circuits are also performed, stability and functionality of the metamaterials are demonstrated. The proposed multi-resonant piezoelectric metamaterials may open new opportunities in vibration mitigation of transport vehicles and underwater equipment.

Keywords: metamaterials, piezoelectric materials, multi-resonance, bandgap, elastic wave isolation

(Some figures may appear in colour only in the online journal)

1. Introduction

Elastic waves in structures are strongly linked to the structural vibration and the consequent noise radiation. Isolating the transmission of elastic waves from sources to other parts of the structures could be an effective method to reduce vibration

and noise. In recent years, elastic metamaterials with local resonators provide new ways to deal with elastic waves, thanks to their subwavelength bandgaps which can prohibit wave propagation. However, the bandgaps of most metamaterials are quite narrow, which cannot meet the engineering requirements in many situations.

An efficient way to extend the overall width of bandgaps in metamaterials are using multiple resonators with different resonant frequencies. In single resonator metamaterials,

* Author to whom any correspondence should be addressed.

each unit cell only has one degree-of-freedom resonating at a unique frequency. Therefore, only one bandgap is created in such metamaterials [1, 2]. For multi-resonator metamaterials, they are composed of unit cells with multiple resonators, the resonance of each resonator could induce one bandgap. This phenomenon is demonstrated by Huang and Sun [3]. They studied a multi-resonator mass-in mass metamaterial, each unit cell of it has two resonance frequencies. Analytical results demonstrate that two bandgaps are observed in the metamaterial. Further investigation reveal that the effective mass of the multi-resonator metamaterials is negative within the two bandgaps. Therefore, by optimizing the parameters of multi-resonator metamaterials to achieve broadband effective mass negativity, broad bandgap can be obtained [4], which is very useful in mitigating blast waves [5, 6]. Generally, increase the number of resonators in the unit cells of multi-resonator metamaterials will obtain wider overall bandgaps. Zhu *et al* [7] designed a layer-in-layer metamaterial, each unit cell has three resonance frequencies, consequently three separated bandgaps are observed. The overall width of bandgaps in multi-resonator metamaterials can be further increased by using damped resonators. Chen *et al* studied a dissipative multi-resonator metamaterial, based on a homogenized model, it is found that the metamaterial utilizes interactions between resonant motions and viscoelastic effects of the damping materials to obtain broadband wave mitigation effects. Effects of such dissipative multi-resonator metamaterial are verified through experimental studies [8]. Introducing internal coupling between different local resonators can also generate multiple resonances to broaden the overall bandgap size. Hu *et al* [9] proposed a modified metamaterial, in which every two unit cells form a group and the two masses in each group are connected by a spring. Multiple bandgaps were generated without adding extra masses due to the interactions between the inner masses. Hu and Tang [10] further used a negative stiffness string to couple the two resonators in a group, ultra-low frequency bandgaps were generated in their research. In summary, multi-resonator metamaterials have wider bandgaps than single resonator metamaterials, they are more practical in mitigating structural vibrations [11–14] or isolating sound transmission [15]. However, currently most of the studied multi-resonator metamaterials are composed of passive resonators. Such passive metamaterials are not adaptive to different working conditions because they are hardly changeable once fabricated.

To overcome the aforementioned limitations of passive metamaterials, piezoelectric metamaterials with tunable effective properties are proposed and attract plenty of study interests. Due to their special electromechanical coupling properties, band gap characteristics of piezoelectric metamaterials, such as size and location, can be tuned by just modifying the shunting circuits. Piezoelectric patches shunted with circuits are first proposed by Forward [16] to damp mechanical vibration. Hagood and Flotow [17] used an inductance in the shunting circuit, it is shown that the inductance and the intrinsic capacitance of the patch form a resonant shunt. Motivated by this finding, Thorp *et al* [18] proposed to periodically place piezoelectric patches shunted with inductance

along a rod. Longitudinal wave bandgap is observed near the resonance frequency of the shunt and can be tuned by changing the inductance value. Airoidi and Ruzzene [19] studied the effective stiffness of a periodic piezoelectric beam shunted with resonant circuits. They found that the effective stiffness shows resonant behaviors near the shunt's resonance frequency, this resonant feature results in bandgaps. Therefore, they proposed that the periodic piezoelectric beam shunted with resonant circuits is a kind of resonant electro-mechanical coupling metamaterials. Following this concept, resonant piezoelectric metamaterials are extended to plates [20–24]. However, due to the nature, resonant piezoelectric metamaterials still have narrow bandgaps. To overcome this drawback, many strategies have been proposed to enlarge the bandgaps. Wang *et al* [25, 26] proposed to add amplifiers into resonant circuits to broaden bandgaps. Gradually varying shunting parameters in space domain to obtain 'rainbow trap' is also used to obtain wave attenuation effect at wider frequency band [27]. Li *et al* [28] designed a self-adaptive circuit to control the resonance frequencies of passive resonator, leading to enlarged low-frequency bandgap. Like passive multi-resonator metamaterials, piezoelectric metamaterials with multiple resonance frequencies are also explored. Airoidi and Ruzzene [29] designed multi-resonant circuits to generate multiple band gaps in a beam. However, these multi-resonant piezoelectric metamaterials are made of analog circuits, which cannot be tuned in real-time and could be very complicated when more than three resonant frequencies are needed.

A recent trend in designing piezoelectric metamaterials is using digital synthetic impedance circuits. Usually, the digital circuit is shunted between the two terminals of a piezoelectric patch. It measures the voltage of the patch and feeds current back to the same patch. The current is feeding according to the transfer function implemented in the digital signal processor. Therefore, a desired impedance between the two terminals of the connected patch is established, which is equal to the inverse of the implemented transfer function. By tuning the implemented transfer function, one can control in real-time the size, location and even number of bandgaps in a piezoelectric metamaterial. Yi *et al* [30] designed programmable metamaterials based on such digital circuits, their simulations and experiments demonstrate that the transfer functions in digital circuits can be programmed in real-time to place bandgaps at locations of different targeted vibration modes. Recently, Sugino *et al* [31] also studied a similar programmable metamaterial beam and verified the tunability of bandgap location via the transfer function. To broaden the overall bandgap size, Sugino *et al* [32] proposed a transfer function to realize multiple resonances in a piezoelectric metamaterial beam. However, their transfer function is only restricted to some specific situation, because it is derived based on beam theory and assuming that the beam is fully covered by the piezoelectric patches. Except the above mentioned digital circuits which use the same patch as sensor and actuator (namely, the patch is working on self-sensing mode), Wang *et al* [33] designed digital circuits using separated patches as sensor and actuator to realize multiple resonances in a piezoelectric metamaterial beam, nonetheless the derived transfer function is also

restricted to beam structures, and may bring instability due to the configurations of separated sensors and actuators.

In this paper, based on self-sensing piezoelectric patches and digital circuits, an appropriate transfer function is derived only using the parameters of the shunted piezoelectric patch, to realize multi-resonant piezoelectric metamaterials with broadened overall bandgap size. Since the transfer function is obtained without using any knowledge of the base structure, to which the shunted piezoelectric patches are bonded, the proposed multi-resonant piezo-metamaterials could be used to design any type of structures, like beams, plates, shells and etc. In this paper, without loss any generality, piezoelectric metamaterial plates are studied to present the design method, analyze the properties of such multi-resonant metamaterials and verify the broadband elastic wave isolation effects. The rest of this paper is organized as follows: in section 2, the transfer function for generating multiple bandgaps is proposed and modified to create bandgaps precisely near the targeted frequencies. section 3 discusses the mechanism of generating multiple bandgaps via the designed transfer function. In section 4, characteristics of bandgaps in the proposed multi-resonant piezo-metamaterials are analyzed. In section 5, broadband isolation of elastic wave propagation is verified based on numerical simulations. In section 6, simulations of metamaterials with digital circuits are performed in time domain to verify the stability. Finally, section 7 presents conclusions of this work.

2. Design of multi-resonant piezoelectric metamaterials

In this section, a piezoelectric metamaterial plate is used as an example to show how the multi-resonant piezoelectric metamaterials are designed. It should be emphasized again that the design method presented using plate-type structure in this section can be directly used to design other type of multi-resonant metamaterial structures, since the designed transfer function for realizing multi-resonance is derived only based on the parameters of piezoelectric patches.

2.1. Physical model of the multi-resonant piezoelectric metamaterial plate

Figure 1 shows the sketch of the designed multi-resonant piezoelectric metamaterial plate. The unit cell of the metamaterial plate is composed of piezoelectric patches bonded on the upper and lower surfaces of a host plate. The polarization of the patches is along the z axis. The patches work as a whole and are assumed to be connected to a digital synthetic impedance circuit, represented by G in figure 1. The surfaces of the patches bonded to the base plate are grounded. Voltage V in the figure is the voltage on the patches' terminals. I means the current flows back to the patches controlled by the digital circuit G . In the digital circuit, a transfer function $G(s)$ is implemented. To make the unit cell generate multiple resonant frequencies at subwavelength scale, the expression of transfer function $G(s)$ is derived in the next section. Geometry and material parameters of the designed unit cell are shown in table 1.

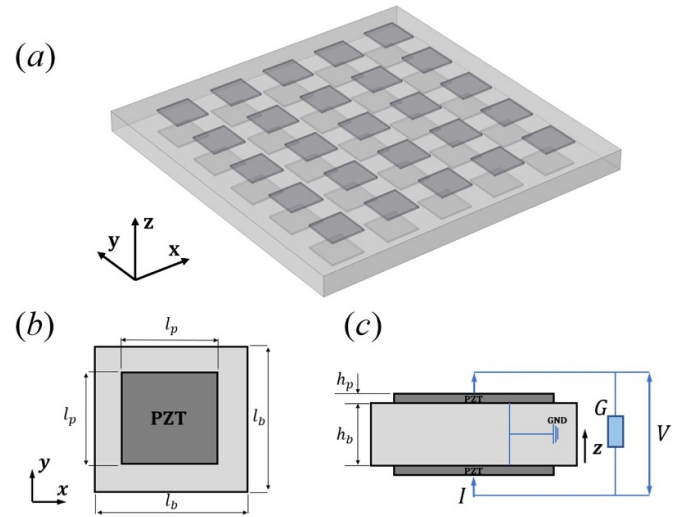


Figure 1. (a) The sketch of the designed piezoelectric metamaterial plate; (b) top view and (c) side view of the unit cell.

Table 1. Geometry and material parameters of the unit cell.

	Plate	Piezoelectric patch
Material	Aluminum	PZT-5 H
Length	$l_b = 33.6$ mm	$l_p = 30.1$ mm
Width	$w_b = 33.6$ mm	$w_p = 30.1$ mm
Thickness	$h_b = 4$ mm	$h_p = 1$ mm
Young's modulus	$Y_b = 70$ GPa	$Y_p = 58.8$ GPa
Density	$\rho_b = 2700$ kg m ⁻³	$\rho_p = 7700$ kg m ⁻³
Coupling constant	—	$d_{31} = -1.7e10$ C/N
Relative permittivity	—	$\epsilon_3^\sigma = 1800$
under constant stress		

2.2. Transfer function for generating multiple resonances

As introduced in appendix A, when piezoelectric patches are shunted with inductance (L), the equivalent in-plane Young's modulus of the patches E_p has a pole (see figure A2). The resonance of E_p consequently results in resonance of the equivalent bending stiffness of the piezoelectric metamaterial plate, creating a bandgap. Inspired by this finding, a transfer function is designed to make E_p resonate at multiple frequencies, namely, have multiple poles. It is expected that the multi-resonances of E_p will generate multiple bandgaps in the metamaterial.

According to the pole assignment method commonly used in the control theory, typically, E_p with multiple poles can be written as

$$E_p = k \frac{\prod_{i=1}^n (s^2 + 2\beta_i \omega_{z,i} s + \omega_{z,i}^2)}{\prod_{i=1}^n (s^2 + 2\beta_i \omega_{p,i} s + \omega_{p,i}^2)} \quad (1)$$

in which, k , β_i , $\omega_{z,i}$, $\omega_{p,i}$ are the gain, damping factor, zeros and poles of the system represented by E_p , respectively. n determines the number of poles and zeros. The poles can be written as $\omega_{p,i} = 2\pi f_i$, in which f_i are the resonance frequencies. It is desired that each resonance frequency will induce one

bandgap around itself, therefore, E_p with n assigned poles may generate n poles at designed locations.

To make the equivalent Young's modulus of a piezoelectric patch has the expression in equation (1), the shunted impedance of the patch must be carefully designed. For a patch shunted with a circuit, whose impedance is expressed as $1/G(s)$, the equivalent Young's modulus of it can be written as

$$E_p = E_p^{sc} \frac{sC_{p3}^T + G(s)}{G(s) + sC_p^T(1 - k_{31}^2)} \quad (2)$$

in which, $k_{31} = d_{31} / \sqrt{S_{11}^E \epsilon_3^\sigma}$ is the extensional coupling factor of the patch, $E_p^{sc} = 1/S_{11}^E$ is the Young's modulus of the patch under short-circuit condition, $C_p^T = A_p \epsilon^\sigma / h_p$ is the intrinsic capacitance of the piezoelectric material at constant stress, A_p is the area of the patch.

According to equations (1) and (2), the transfer function can be derived as

$$G(s) = sC_{p3}^T \frac{\prod_{i=1}^n (s^2 + 2\beta_i \omega_{p,i} s + \omega_{p,i}^2) - \prod_{i=1}^n (s^2 + 2\beta_i \omega_{z,i} s + \omega_{z,i}^2)}{\frac{1}{1-k_{31}^2} \prod_{i=1}^n (s^2 + 2\beta_i \omega_{z,i} s + \omega_{z,i}^2) - \prod_{i=1}^n (s^2 + 2\beta_i \omega_{p,i} s + \omega_{p,i}^2)} \quad (3)$$

Note that, in the derivation of equation (3), the gain k in equation (1) is chosen to be $k = E_p^{sh} / (1 - k_{31}^2)$ in order to ensure that the order of the numerator is not greater than that of the denominator in the transfer function. Besides, the poles of the transfer function must all be in the left half plane of the complex domain, which drops the restrictions in equation (4) on the assigned zeros and poles

$$\omega_{z,i} < \omega_{p,i} < \left(\frac{1}{1 - k_{31}^2} \right)^{\frac{1}{2n}} \omega_{z,i}, \quad i = 1, 2, \dots, n. \quad (4)$$

The transfer function $G(s)$ in equation (3) is enough to generate multiple bandgaps in piezoelectric metamaterials. However, the bandgap locations will deviate from the placed poles. A modification to the transfer function is made in section 2.3 to eliminate this deviation.

2.3. Modification of the transfer function

In practical applications, usually the frequencies at where the vibration needs to be controlled are known. The transfer function should be designed to precisely create bandgaps at these resonant frequencies. Therefore, it is highly desired

that the bandgap locations are just around the assigned poles in the transfer function. As introduced in appendix B, a numerical method is used to predict the bandgap regions. It is observed that when the original transfer function in equation (3) is used, the generated bandgaps locate away from the designed poles (see figures 2(a) and (b)), a modification procedure is performed to improve its accuracy.

Figures 2 (a) and (b) shows the bandgaps generated by the original transfer function. In figure 2(a), the transfer function only has one pole (indicated by the dot-dash line in the figure), a single bandgap is observed at frequency higher than the assigned pole. In figure 2(b), two poles are assigned in the transfer function, therefore two bandgaps are observed from the dispersion curves, they are also higher than the corresponding assigned poles. From figures 2 (a) and (b), it can be concluded that the designed transfer function in equation (3) can actually generate multiple bandgaps. However, there are deviations exist between the obtained bandgap locations and assigned poles.

To eliminate these deviations, the transfer function in equation (3) is multiplied by a gain γ , the modified transfer function is expressed as

$$G(s) = s\gamma C_{p3}^T \frac{\prod_{i=1}^n (s^2 + 2\beta_i \omega_{p,i} s + \omega_{p,i}^2) - \prod_{i=1}^n (s^2 + 2\beta_i \omega_{z,i} s + \omega_{z,i}^2)}{\frac{1}{1-k_{31}^2} \prod_{i=1}^n (s^2 + 2\beta_i \omega_{z,i} s + \omega_{z,i}^2) - \prod_{i=1}^n (s^2 + 2\beta_i \omega_{p,i} s + \omega_{p,i}^2)} \quad (5)$$

by varying the gain γ , the locations of bandgaps can be adjusted. Therefore, if a suitable γ is chosen, the bandgaps can be placed around the assigned poles.

For a piezoelectric metamaterial plate whose parameters are all known, the gain γ is chosen through the following procedure. A single pole is assigned in the transfer function,

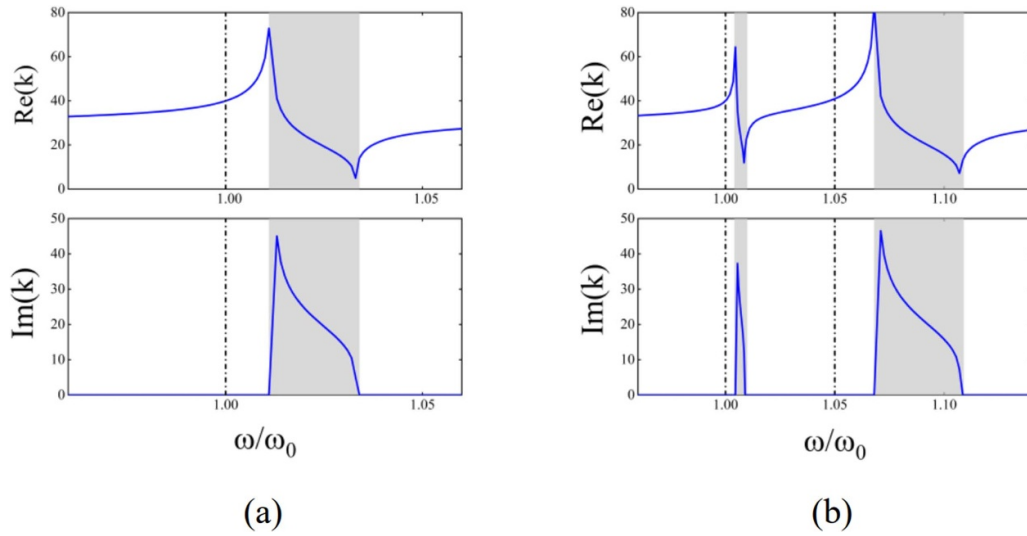


Figure 2. The bandgaps obtained from the original transfer function. (a), (b): single bandgap and multiple bandgaps generated by the original transfer function. The shadowed areas indicate the bandgap regions, the black dot–dash line indicates the normalized poles used in the transfer functions.

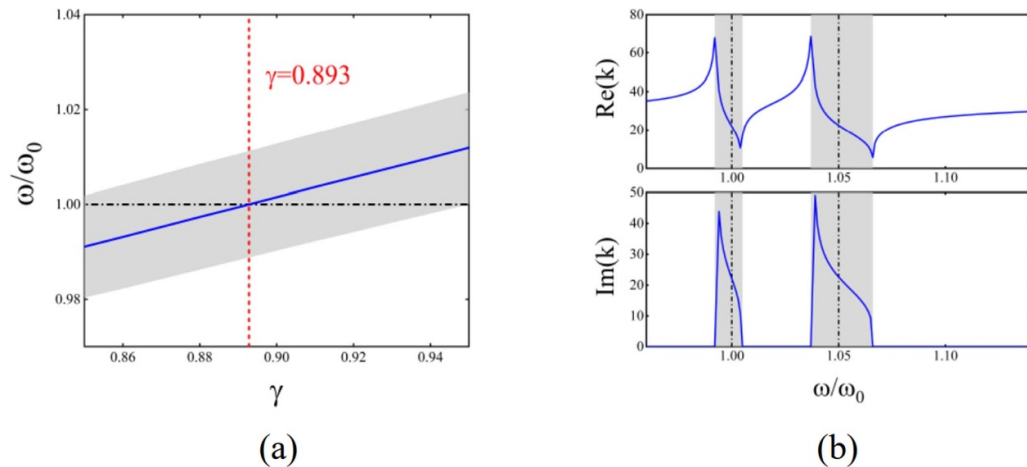


Figure 3. (a) The bandgap location varies with gain γ , the blue line indicates the bandgap center at different γ . (b) Multiple bandgaps precisely generated by the modified transfer function.

varying γ to adjust the location of the bandgap, chose the γ for the modified transfer function when the pole is at the center of the bandgap, as illustrated in figure 3(a). In figure 3(b), it is verified that even though the value of γ is chosen using one pole in the transfer function, the modified transfer function can precisely generate multiple bandgaps just around the designed poles.

If the geometry or material parameters of a metamaterial plate are changed, the gain γ in the modified transfer function must be re-chosen. Figure 4 shows the required gain γ for different covering ratio χ and thickness ratio h_r , in which $\chi = (l_p/l_b)^2$ is the coverage ratio of the patch in the unit cell, and $h_r = h_p/h_b$ is the thickness ratio between the patch and the host plate. One can clearly see that γ strongly depends on these geometry parameters. If varying the material parameters, gain γ correspondingly will also change.

3. Mechanism of generating multiple bandgaps

For passive resonant metamaterials or piezoelectric metamaterials with inductance, the bandgaps are caused by negative effective parameters of the metamaterials [34, 35]. To explain how the proposed transfer function can create multiple bandgaps, the effective bending stiffness of the multi-resonant piezo-metamaterial plate is studied in this section.

3.1. Analytical expression of the effective bending stiffness of the metamaterial plate

Equivalent bending stiffness of the unit cell shown in figure 1 can be written as [19]

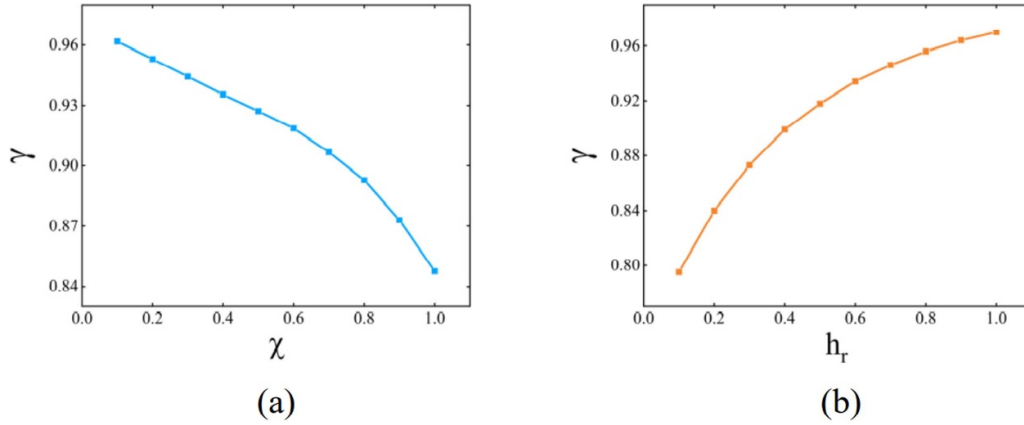


Figure 4. The effects of geometry parameters on gain γ in the modified transfer function. (a) gain γ varies with coverage ratio χ when $h_r = 0.25$; (b) gain γ varies with thickness ratio h_r when $\chi = 0.8$.

$$D_{\text{eff}} = \frac{D_A D_b}{(1 - \chi) D_A + \chi D_b} \quad (6)$$

in which, $D_b = E_b h_b^3 / 12 (1 - \nu_b^2)$ is the bending stiffness of the bare plate, and D_A represents the equivalent bending stiffness of the middle sandwich part of the unit cell, expression of it is

$$D_A = D_b + \frac{2E_p}{3(1 - \nu_p^2)} \left[\left(\frac{h_b}{2} + h_p \right)^3 - \left(\frac{h_b}{2} \right)^3 \right]. \quad (7)$$

In equation (7), ν_p is the equivalent Poisson's ratio of the shunted piezoelectric patch, it is expressed as

$$\nu_p = \nu_p^{sc} \frac{G(s) + sC_p^T (1 + k_{31}^2 / \nu_p^{sc})}{G(s) + sC_p^T (1 - k_{31}^2)} \quad (8)$$

in which, $\nu_p^{sc} = -S_{12}^E / S_{11}^E$ is the Poisson's ratio of the patch under short-circuit condition.

According to equations (2), (6)–(8), one can deduce the detailed expression of the equivalent bending stiffness of the unit cell, which is

$$D_{\text{eff}} = \frac{D_b \left[D_b + D_p^{sc} + D_p^{sc} \frac{sC_p^s k_{31}^2 (1 + \nu_p^{sc})}{(1 - k_{31}^2)(1 - \nu_p^{sc}) [G(s) + sC_p^s] - sC_p^s k_{31}^2 (1 + \nu_p^{sc})} \right]}{D_b + (1 - \chi) D_p^{sc} \left[1 + \frac{sC_p^s k_{31}^2 (1 + \nu_p^{sc})}{(1 - k_{31}^2)(1 - \nu_p^{sc}) [G(s) + sC_p^s] - sC_p^s k_{31}^2 (1 + \nu_p^{sc})} \right]} \quad (9)$$

in which, $D_p^{sc} = E_p^{sc} [(h_b + 2h_p)^3 - h_b^3] / 24 (1 - \nu_p^{sc2})$ is the equivalent bending stiffness of the piezoelectric sandwich structure under short-circuit condition. $C_p^s = C_p^T (1 - k_{31}^2)$ is the intrinsic capacitance of the patch under constant strain.

3.2. Comparison between the bandgap and negative bending stiffness regions

Figures 5(a) and (b) compare the negative bending stiffness regions obtained using equation (9) with bandgap regions predicted using the numerical method for single-pole and multi-poles cases. It can be observed that there is a consistent one-to-one match between each negative bending stiffness region and each bandgap. However, these two regions are not well overlapped, the negative bending stiffness regions are at higher frequencies than the numerically predicted bandgaps. If these differences can be eliminated, one can conclude without doubt that the multiple bandgaps are generated because the designed

transfer function make the effective bending stiffness of the metamaterial plate be negative at multiple frequency bands.

Previous studies demonstrate that the analytical model will misestimate the intrinsic capacitance of a piezoelectric patch compared with the numerical model. Therefore, one can try to eliminate the deviations shown in figures 5(a) and (b) by correcting the analytical capacitance. When the analytical capacitance is corrected to be $C_p^{s*} = 0.958 C_p^s$, the analytical negative bending stiffness regions and the numerical bandgaps are well consistent with each other, as illustrated in figures 5(c) and (d). Therefore, the conclusion considering the mechanism of generating multi-bandgaps by the proposed transfer function drew at the end of the previous paragraph is solid.

4. Characteristics of multiple bandgaps

In this section, characteristics of the multiple bandgaps generated by the transfer function are studied. These bandgaps

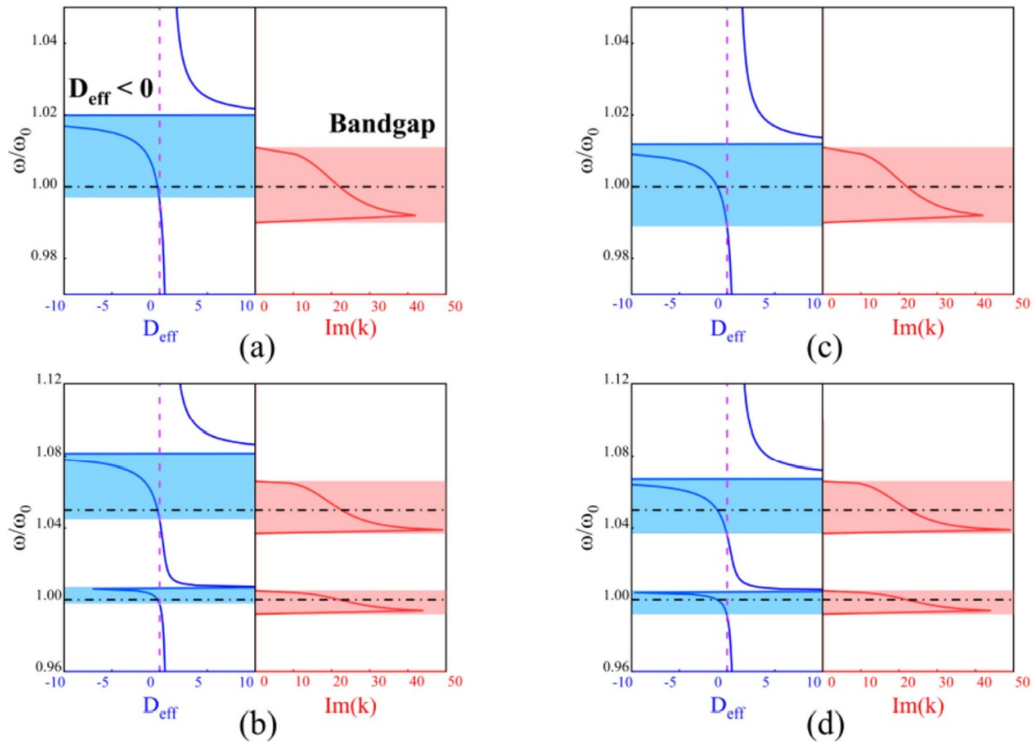


Figure 5. Comparison between the analytical negative bending stiffness regions and the bandgaps predicted using the numerical method. (a), (b): before correcting the analytical intrinsic capacitance; (c), (d): after correcting the analytical intrinsic capacitance. In each figure, the blue shadowed areas indicate the negative bending stiffness regions, the red shadowed areas indicate the bandgap regions, the horizontal dot–dash lines are the assigned poles.

are predicted by the negative bending stiffness regions using equation (9) with the corrected intrinsic capacitance C_p^s . Two phenomena are observed when distances between bandgaps varies, they are presented and discussed below.

4.1. Bandgap coupling phenomenon

When the distance between two bandgaps decreases, interaction effects between them are observed, which indicates that these bandgaps are coupled with each other. To study such coupling phenomena, a transfer function with two poles is used, the first pole is ω_0 , the second one is ω_1 here, $\omega_1 = (1 + \alpha)\omega_0$ and α is a constant, it is used to adjust the distance between these two poles. The transfer function will generate two bandgaps in the metamaterial plate, the first one will be around ω_0 , and the second one will be around ω_1 . On the other hand, in order to demonstrate the coupling phenomena, the bandgap generated by a transfer function with a single pole ω_0 or ω_1 is used as reference.

Variations of the first and second bandgap widths when α increases from 0 to 0.25 are studied in figure 6. When the transfer function has a single pole ω_0 and ω_1 , respectively, the generated two bandgaps have no interaction with each other, namely they are uncoupled. When the transfer function has two poles ω_0 and ω_1 simultaneously, the generated two bandgaps affect each other, namely they are coupled. By comparing the coupled bandgaps with the uncoupled ones, it can be seen from figure 6 that, as the distance between the two poles decreases, the first bandgap generated by the two-pole transfer

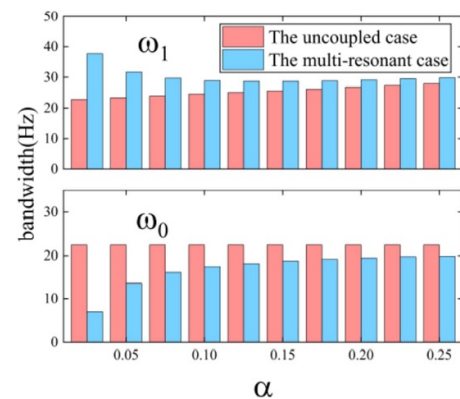


Figure 6. Variations of the widths of the first and second bandgaps generated by the two-pole transfer function when α increases from 0 to 0.25. Bandgap widths of the uncoupled case are also illustrated in the figure as references.

function shrinks, on the contrary, the second bandgap generated by the two-pole transfer function enlarges. The shrinking and enlarging trends become more obvious when the two poles are closer, which indicates that the coupling effects between bandgaps become stronger.

Since the coupling phenomenon narrows the first bandgap and broadens the second one, it is worth to find out how the total bandwidth is influenced by the coupling effect. Besides, the total bandwidth is a very important index when metamaterials are designed for broadband elastic wave isolation. The

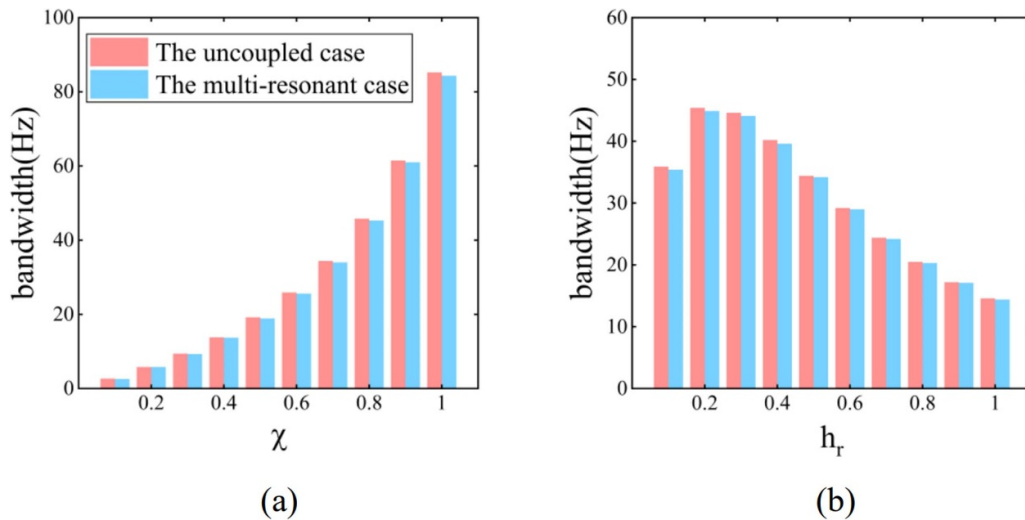


Figure 7. Variation of the total bandwidth of the bandgaps generated by the two-pole transfer function with (a) covering ratio χ when $h_r = 0.25$ and (b) thickness ratio h_r when $\chi = 0.8$. The $\alpha = 0.05$ in the simulations. In these figures, variation of the widths of the two uncoupled bandgaps are also illustrated as references.

total bandwidth of the two bandgaps generated by the two-pole transfer function is compared with the sum of the two uncoupled bandgaps for different geometry parameters, the results are illustrated in figure 7. In this case, the distance between the two poles is $\alpha = 0.05$. It can be seen that the coupled bandgaps as a whole is almost as large as the sum of the corresponding uncoupled bandgaps. These results also make clear that our multi-bandgap metamaterials have significant advantages compared with those obtained using ‘rainbow’ strategy [30]. In the ‘rainbow’ design, to generate multiple bandgaps, one need to connect the patches in different unit cells to shunt with different resonance frequencies. In such a manner, each unit cell will generate one bandgap, and these bandgaps could be considered as uncoupled. However, the required number of unit cells will significantly increase in order to obtain multiple bandgaps. For the metamaterials proposed in this paper, the multiple bandgaps are generated by digital shunts with specially designed transfer function, namely, each unit cell is participating in creating all the bandgaps. Therefore, the number of unit cell do not need to be increased. In addition, the total bandwidth of the bandgaps is almost the same as those obtained using the ‘rainbow’ design.

4.2. Bandgap merging phenomenon

As introduced in the above section, when the bandgaps get closer to each other, the coupling effect between them becomes more obvious, which narrows the first bandgap and broadens the second one. An interesting phenomenon occurs when the bandgaps are close enough, the two bandgaps merge into one, resulting in a bandgap which could be wider than both the two original bandgaps. This bandgap merging phenomenon is studied in this section.

Bandgaps will merge into one when the distances between the poles in the transfer function are smaller than a critical value. To demonstrate such phenomenon, a two-pole transfer

function is used to generate two bandgaps. The poles are ω_0 and ω_1 as aforementioned. Figure 8(a) demonstrates that, when α is relatively large, two separated bandgaps I and II are generated; when α is smaller than a critical value 0.021, the two bandgaps merge into a single one. Figure 8(b) compares the band width of the merged bandgap with the widths of the separated two, it is observed that when α is equal to or just a little bit smaller than the critical value 0.021, the merged bandgap is almost as wide as the sum of the two separated bandgaps.

Bandgaps generated by transfer functions with more than two poles will also coalesce as long as the distance between any two of these poles is equal to or smaller than the critical value. Therefore, one can use this merging phenomenon to obtain a broad bandgap. Figure 9 compares the width of the merged bandgaps when different numbers of poles are involved. It is observed that the bandgap becomes wider when the number of involved poles increases.

The critical distances between poles in the transfer function determines when bandgaps merge into one, such values depend on the geometry and material parameters of the metamaterial unit cell. Figures 10(a) and (b) illustrates the influences of the geometry parameters on the critical value of α . It can be seen that the critical value is almost the same when $\chi \geq 0.7$ and $h_r \leq 0.5$, when $\chi < 0.7$, one need to recalculate the critical value if the covering ratio is changed. Besides, when $h_r > 0.5$, the critical value needs to be re-corrected if the thickness ratio is changed as well.

5. Numerical verification of the broadband elastic wave isolation effects

In this section, the broadband elastic wave isolation effects of the multi-resonant piezoelectric metamaterials are numerically verified. Figure 11 shows the studied piezoelectric metamaterial plate modeled in COMSOL. The metamaterial plate is composed of 12×12 unit cells. Geometry and material

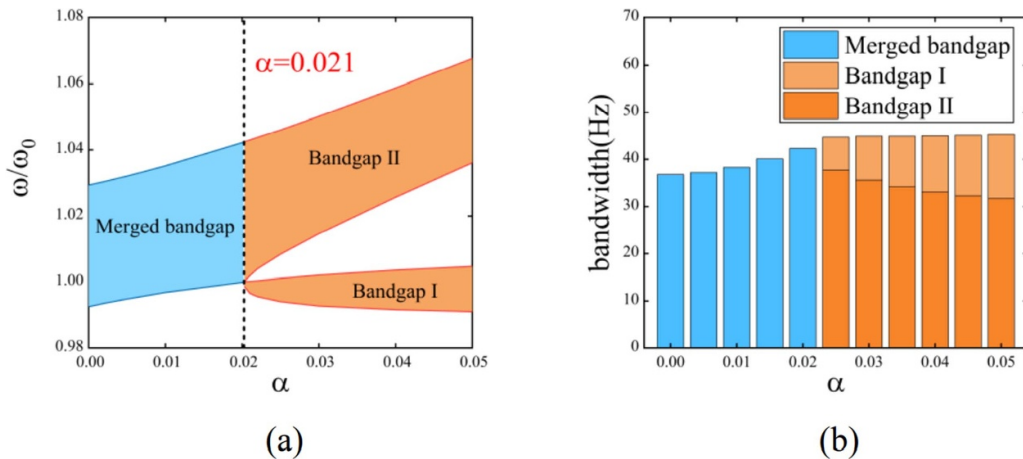


Figure 8. (a) Illustration of the bandgap merging phenomenon as two poles get close. (b) Comparison between the widths of the merged bandgap and the separated ones.

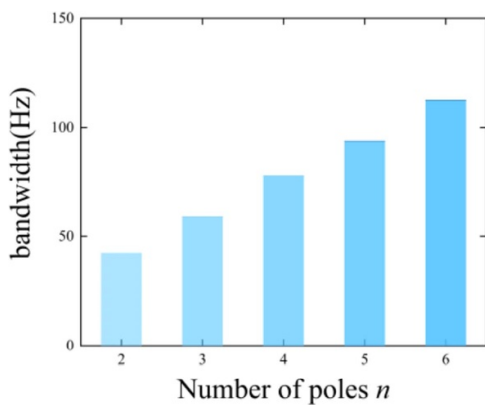


Figure 9. Influences of the number of poles in the transfer function on the width of the merged bandgap.

parameters of one unit cell are the same as those in table 1. A harmonic load F is applied at point A to mimic a source of disturbance. The transverse vibration responses at a far-field point B in frequency domain are measured, they are divided by the amplitude of the excitation force, results in the frequency-response function of point B, which characterizes the transmission of vibration from the source to the remote part of the plate in frequency domain.

5.1. Elastic wave isolation effects of multiple separated bandgaps

In many practical situations, the vibration is caused by unbalanced rotators. The spectrum of such disturbance has distinct lines. Besides, the locations of these lines depend on the rotate speed, which varies in different working conditions. Therefore, it is required not only that the structural vibration transmission at multiple line frequencies should be isolated, and also the isolating effects can be tuned according to working conditions. Our proposed multi-resonant piezoelectric metamaterials can meet such demands. To demonstrate the vibration (wave) transmission isolation effects in

the metamaterial plate, three cases are studied with different transfer functions. In each case, particular line frequencies are chosen as targeted frequencies, these frequencies are used as poles to design the corresponding transfer function. Parameters of the designed transfer functions in these three cases are summarized in table 2. The vibration transmission properties between the source A and the observation point B in these three cases are illustrated in figure 12. It is clearly demonstrated that by properly design the transfer function, transmission of vibration at targeted line frequencies can be effectively prohibited in the structure.

It should be noted that, the distances between the bandgaps in the three cases illustrated in figure 12 are far, the coupling effects between them are weak. When targeted line frequencies are close, the designed bandgaps will be close to each other, the coupling effect between bandgaps may make the lower one shrink, a probable consequence could be that this bandgap is too narrow to isolate the vibration transmission. In such situations, the coupling effects between bandgaps should be considered when designing the transfer function.

5.2. Elastic wave isolation effects of merged broad bandgaps

In other situations, the external stimulations have wide spectrums, to isolate the structural vibration caused by them, a broad bandgap is demanded. Exploring the bandgap merging phenomenon, it is possible to generate a wide bandgap. To verify the broadband vibration transmission isolation effects of the merged bandgaps, cases 4 and 5 are studied, poles of the used transfer function are listed in table 2. Figure 13 shows the vibration transmission properties between the source A and the observation point B in these 2 cases. It can be seen that the bandgap generated by one pole can only isolate the vibration of one mode (case 4). When multiple poles are assigned and carefully designed to obtain a merged broad bandgap, vibration of two modes can be isolated (case 5). One can further add poles into the transfer function to increase the effective frequency band.

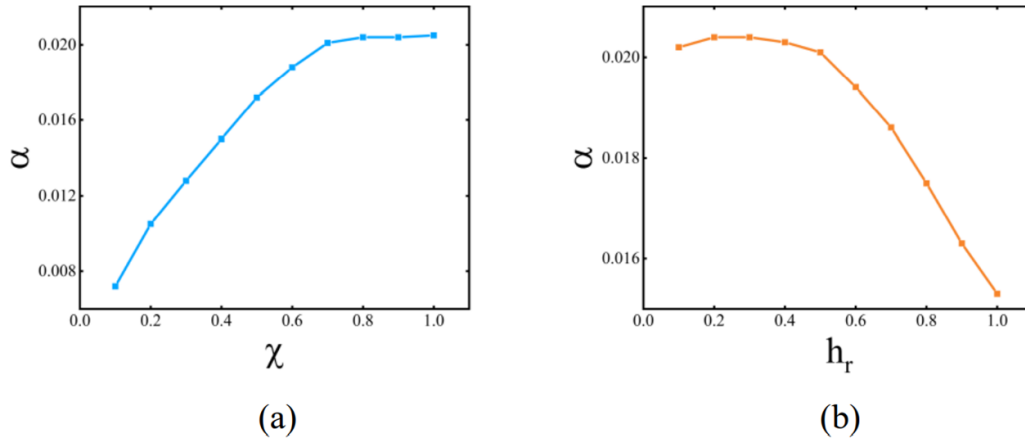


Figure 10. Variation of the critical value along with the (a) covering ratio χ when $h_r = 0.25$ and (b) thickness ratio h_r when $\chi = 0.8$.

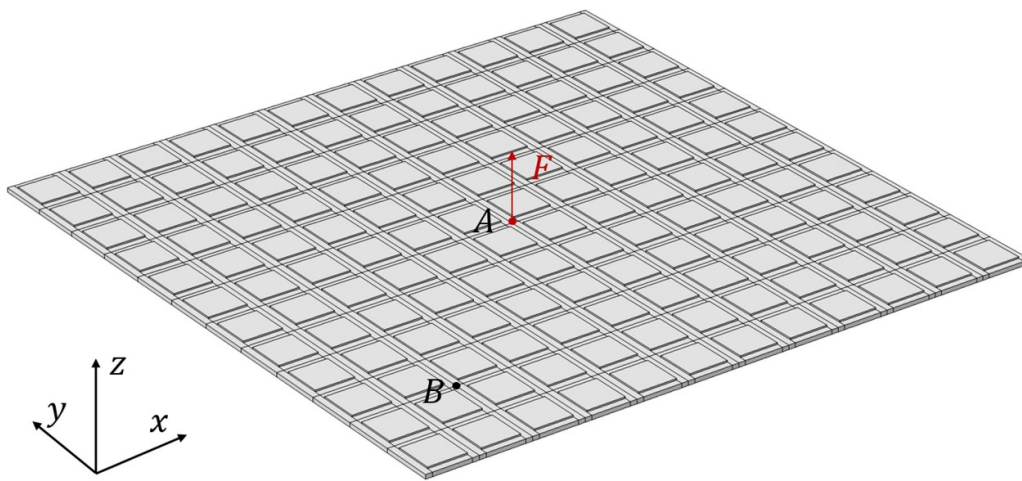


Figure 11. The sketch of the metamaterial plate in the numerical simulation.

Table 2. Poles of the transfer functions used in different cases, $\omega_{p,i} = 2\pi f_i$.

		Poles number n	Resonant frequencies f_i (Hz)
Multiple separate bandgaps	Case 1	2	1056, 1756
	Case 2	3	1056, 1756, 2148
	Case 3	5	764, 1056, 1756, 1868, 2148
Merged broad bandgaps	Case 4	1	1756
	Case 5	5	1750, 1755, 1760, 1770, 1780

6. Time domain simulations of multi-resonant piezoelectric metamaterials with digital circuits

To further prove the stability and functionality of the proposed multi-resonant metamaterials, in this section, time domain simulations accounting for the full dynamics of

the metamaterials with digital circuits are done in Simulink. The digital circuit originally proposed by Fleming *et al* [36] is used here, it can be modelled in Simulink using Simscape Electronics, as shown in figure 14. The proposed transfer function $G(s)$ for generating multi-resonances is implemented in the digital circuit during time domain simulations.

Since the proposed transfer function can be used to design any type of multi-resonant metamaterials, in this section, a two-step piezoelectric metamaterial beam shown in figure 15 is considered instead of the metamaterial plate used in section 5. The beam is composed of 10 and a half cells, the geometry parameters of one unit cell are listed in table 3. There are two segments with different thickness in each unit cell, and the patches for control are glued on the thin segment, they are connected to the digital circuit (represented by G in figure 15), which measures the voltage V_c as input signal and feedbacks current I_c as output signal. The beam is excited by the patches in the half cell with applied voltage V_e . The acceleration along z axis at the red point in the right end is studied.

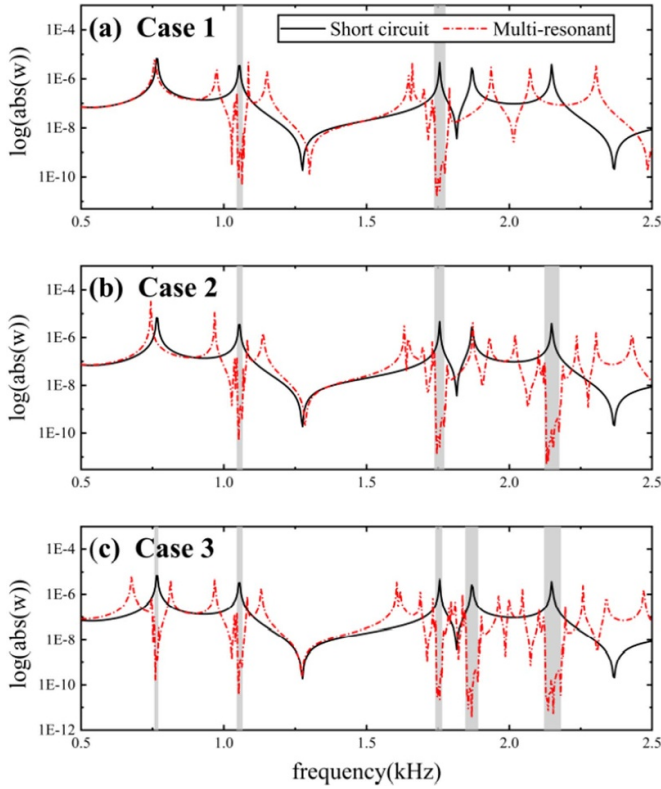


Figure 12. Frequency-response curves at point B in simulated cases 1–3.

The two-step metamaterial beam is first modeled using the finite element method, then, the model is reduced applying the modal synthesis method. The reduced model is:

$$\begin{aligned} M\ddot{\mathbf{q}} + C_d\dot{\mathbf{q}} + K\mathbf{q} + H_{dv} \begin{bmatrix} V_e \\ V_c \end{bmatrix} &= \mathbf{f} \\ -H_{dv}^T\dot{\mathbf{q}} + C_p \begin{Bmatrix} \dot{V}_e \\ \dot{V}_c \end{Bmatrix} &= - \begin{Bmatrix} I_e \\ I_c \end{Bmatrix} \end{aligned} \quad (10)$$

in which, \mathbf{q} is a vector contains the modal coordinates, which is associated with the mechanical displacements \mathbf{d} through $\mathbf{d} = \Phi\mathbf{q}$, with Φ being a matrix composed of column vectors representing the modes of the two-step beam when all the patches are short circuited; V_e and V_c represents voltages of the patches for excitation and voltages of the patches for control, respectively; M , C_d and K are the modal mass matrix, damping matrix and stiffness matrix, respectively; $H_{dv} = [H_{dve} \ H_{dvc}]$ is the modal coupling matrix, the diagonal elements of $C_p = \begin{bmatrix} C_{pee} & \mathbf{0} \\ \mathbf{0} & C_{pcc} \end{bmatrix}$ represent the intrinsic capacitances of the patches for excitation or for control; \mathbf{f} represents the modal mechanical excitation, which is zero in this study; I_e and I_c are the currents flow into the patches for excitation and patches for control, respectively.

To model the two-step metamaterial beam in Simulink, the governing equations in Equation are further re-written into the state-space form as:

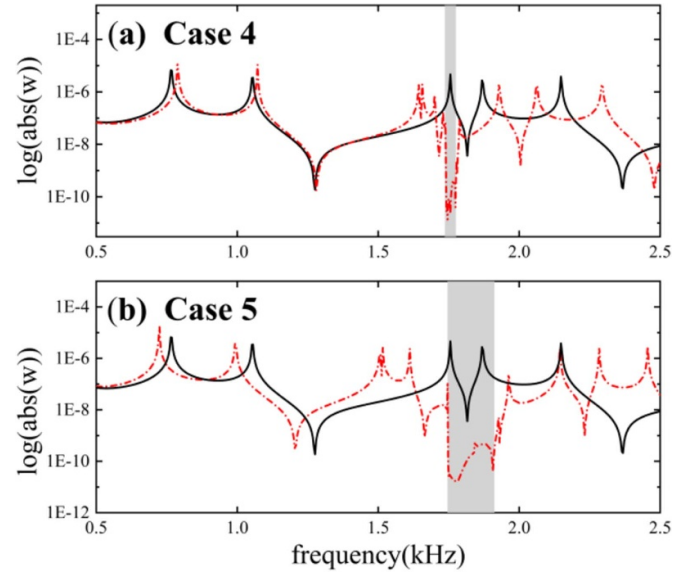


Figure 13. Frequency-response curves at point B in simulated cases 4 and 5.

$$\begin{aligned} \dot{\mathbf{x}} &= \mathbf{A}\mathbf{x} + \mathbf{B}\mathbf{u} \\ \mathbf{y} &= \mathbf{C}\mathbf{x} + \mathbf{D}\mathbf{u} \end{aligned} \quad (11)$$

in which, $\mathbf{x} = [\dot{\mathbf{q}} \ \mathbf{q} \ V_c]^T$ is the state variable vector, $\mathbf{u} = [\mathbf{f} \ V_e \ \dot{V}_e \ I_c]^T$ and $\mathbf{y} = [\mathbf{q} \ V_c]^T$ are the input vector and output vector of the system, respectively; \mathbf{A} , \mathbf{B} , \mathbf{C} and \mathbf{D} are four matrices, details of them are:

$$\begin{aligned} \mathbf{A} &= \begin{bmatrix} -M^{-1}C_d & -M^{-1}K & -M^{-1}H_{dvc} \\ \mathbf{0} & \mathbf{0} & \mathbf{0} \\ C_{pcc}^{-1}H_{dvc}^T & \mathbf{0} & \mathbf{0} \end{bmatrix}, \\ \mathbf{C} &= \begin{bmatrix} \mathbf{0} & \mathbf{1} & \mathbf{0} \\ \mathbf{0} & \mathbf{0} & \mathbf{1} \end{bmatrix} \\ \mathbf{B} &= \begin{bmatrix} M^{-1} & -M^{-1}H_{dve} & \mathbf{0} & \mathbf{0} \\ \mathbf{0} & \mathbf{0} & \mathbf{0} & \mathbf{0} \\ \mathbf{0} & \mathbf{0} & \mathbf{0} & -C_{pcc}^{-1} \end{bmatrix}, \\ \mathbf{D} &= \begin{bmatrix} \mathbf{0} & \mathbf{0} & \mathbf{0} & \mathbf{0} \\ \mathbf{0} & \mathbf{0} & \mathbf{0} & \mathbf{0} \end{bmatrix}. \end{aligned} \quad (12)$$

The primary block diagram in Simulink is shown in figure 16. The highlighted block contains ten identical subsystems representing the digital circuits connected to the two-step metamaterial beam. Note that, details of the subsystems are illustrated in figure 14.

In all the simulations, the remained number of modes is 20 to ensure convergence of the reduced model in equation (10). A white noise signal is used as the input (namely the excitation voltage). Transverse acceleration of the selected point (the red point in figure 15) can be obtained from the output. A transfer function designed to generate 5 bandgaps are implemented. The excitation voltage and the calculated acceleration signal

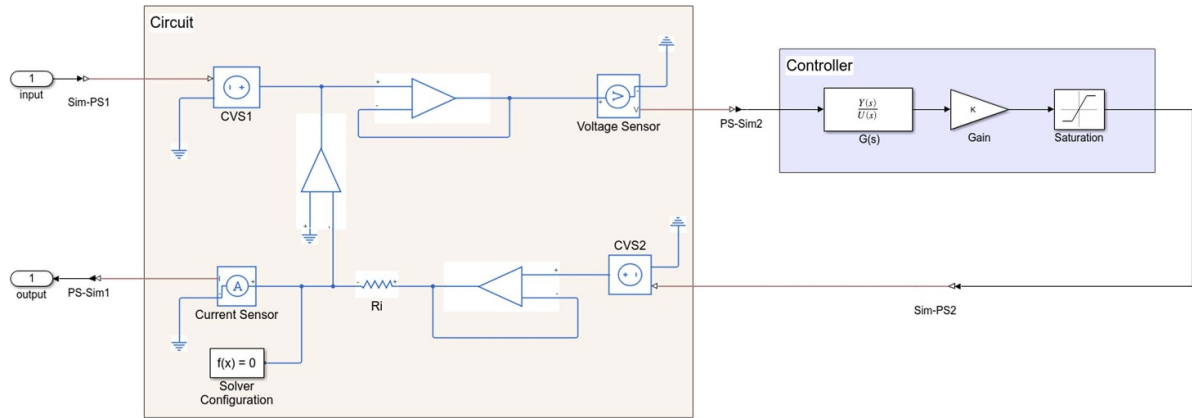


Figure 14. Block diagram showing the digital circuit. The input to the circuit is the voltage across the piezoelectric patches for control, V_c ; the output is the current flow to the patches, I_c .

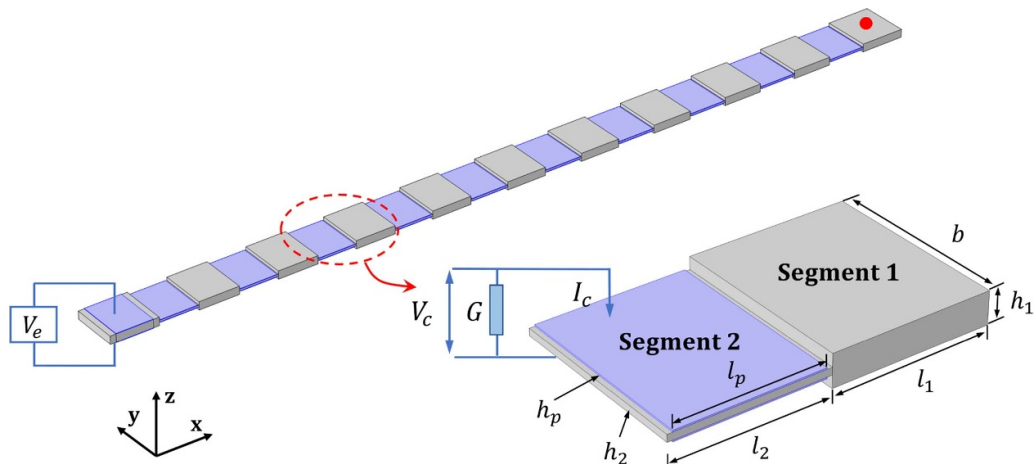


Figure 15. Schematics of the two-step piezoelectric metamaterial beam with digital circuits.

Table 3. Geometrical parameters of one unit cell.

Parameter	Variable
Length of the patch	$l_p = 45\text{mm}$
Thickness of the patch	$h_p = 0.5\text{ mm}$
Width	$b = 60\text{mm}$
Length of segment 1	$l_1 = 52.1\text{ mm}$
Length of segment 2	$l_2 = 49.3\text{ mm}$
Thickness of segment 1	$h_1 = 10.1\text{ mm}$
Thickness of segment 2	$h_2 = 2.2\text{ mm}$
Total length of the beam	$l_{\text{tot}} = 1065.3\text{ mm}$

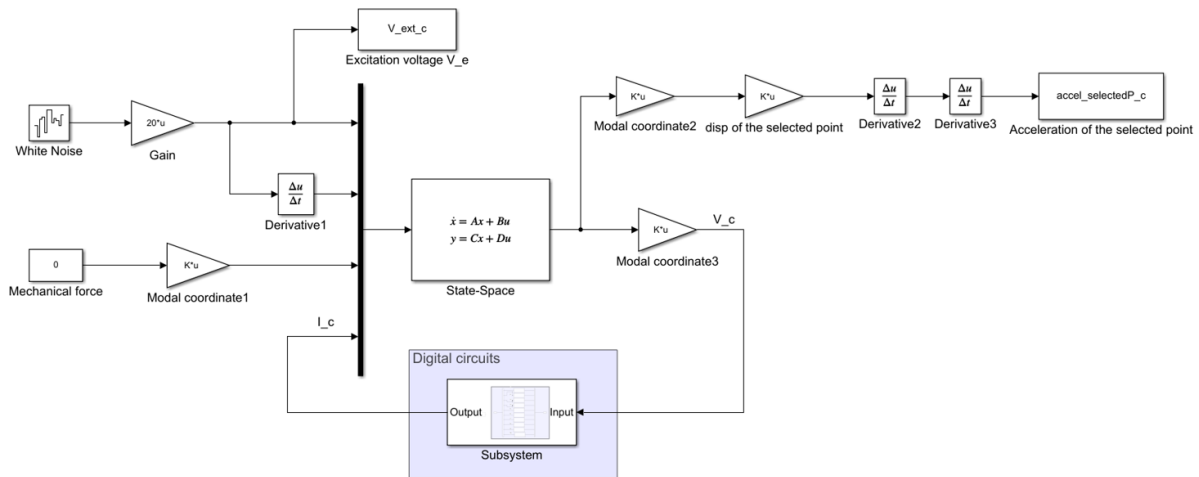


Figure 16. Simulink block diagram for metamaterial with digital circuits in modal coordinates.

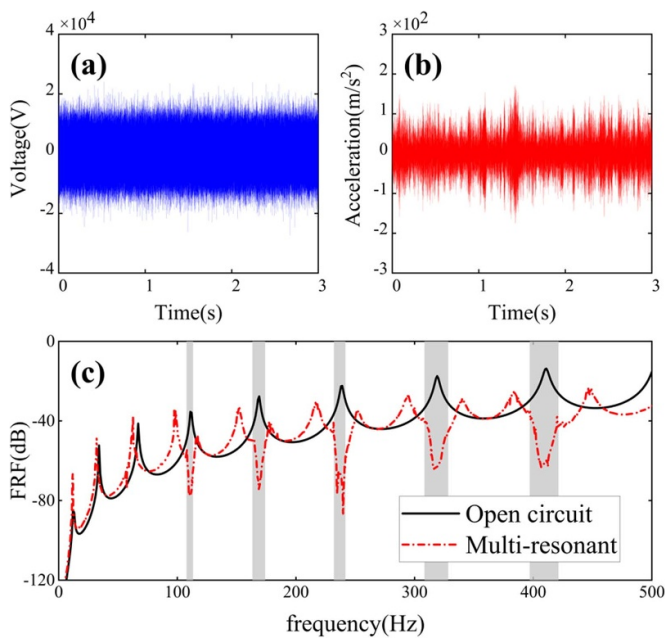


Figure 17. (a) The white noise voltage used for excitation. (b) The calculated transverse acceleration of the selected point. (c) FRFs relating the excitation voltage and acceleration response, shadowed areas indicate the designed bandgaps.

in time domain are shown in figures 17(a) and (b), respectively. By using a Hanning window and the fast Fourier transform, the frequency response function (FRF) relating the excitation voltage and the acceleration is obtained, which is shown in figure 17(c). Results in figure 17 clearly demonstrate that the proposed multi-resonant metamaterials are stable in time domain and work well in the way they are designed to be.

7. Conclusions

In this paper, a general transfer function is designed to realize multi-resonant piezoelectric metamaterials based on self-sensing piezoelectric patches and digital circuits. The transfer

function is designed by only using the parameters of patches, therefore, it can be used to realize any type of multi-resonant metamaterial structures, like beams, plates and shells. By analytically studying the effective bending stiffness of a multi-resonant piezo-metamaterial plate, it is shown that the transfer function makes the effective bending stiffness be negative in multiple frequency ranges, leading to multiple bandgaps. The characteristics of these multiple bandgaps are further investigated. As the distances between the bandgaps decrease, coupling phenomena between the bandgaps are observed. When the distances are less than a critical value, the bandgaps will merge into one, results in a broad bandgap. Next, the structural vibration transmission (namely, elastic wave) isolation effects in the multi-resonant piezo-metamaterials are studied, it is demonstrated that, by designing the transfer function, transmission of vibration at multiple line frequencies or within a broad frequency band can be efficiently prohibited in the structure. Finally, the simulations of metamaterials with digital circuits are performed in time domain, good stability and functionality of the proposed metamaterials are verified. Hopefully, this new type of multi-resonant piezoelectric metamaterials could open new opportunities in vibration mitigation of transport vehicles and underwater equipment. Next step work will focus on the influences of damping induced by the transfer function on the bandgaps and vibration isolation effects, such influences are ignored in this paper.

Data availability statement

The data that support the findings of this study are available upon reasonable request from the authors.

Acknowledgments

This work is supported by the Innovation Foundation of Maritime Defense Technologies Innovation Center (No. JJ-2020-719-05), National Key Research and Development Program of China (2021YFE0110900) and National Natural Science

Foundation of China (No. 11991030, No. 11991031 and No. 11872112).

Appendix A. Intrinsic connection between the bandgap of a piezoelectric metamaterial plate shunted with inductance and the equivalent Young's modulus of the shunted piezoelectric patch

When a piezoelectric patch is shunted with only inductance L , the equivalent bending stiffness of the unit cell in figure 1 is written as

$$D_{\text{eff}} = \frac{D_b \left[D_b + D_p^{\text{sc}} - D_p^{\text{sc}} \frac{\omega^2 k_{31}^2 (1 + \nu_p^{\text{sc}})}{(1 - k_{31}^2)(1 - \nu_p^{\text{sc}})(\omega_{LC}^2 - \omega^2) + \omega^2 k_{31}^2 (1 + \nu_p^{\text{sc}})} \right]}{D_b + (1 - \chi) D_p^{\text{sc}} \left[1 - \frac{\omega^2 C_p^{\text{sc}} k_{31}^2 (1 + \nu_p^{\text{sc}})}{(1 - k_{31}^2)(1 - \nu_p^{\text{sc}})(\omega_{LC}^2 - \omega^2) + \omega^2 k_{31}^2 (1 + \nu_p^{\text{sc}})} \right]} \quad (\text{A.1})$$

in which, $\omega_{LC} = 1 / \sqrt{LC_p^{\text{sc}}}$ is the resonance frequency of the shunt.

Figure A1 shows the variation of the equivalent bending stiffness when the frequency changes. In the figure, $f_0 = \omega_{LC} / 2\pi$. It can be seen that the equivalent bending stiffness shows resonant feature near the resonance frequency of the shunt, leading to a frequency region with negative bending stiffness, as indicated in figure A1. It is well known that the negative bending stiffness region corresponds to a bandgap.

Now, consider the equivalent Young's modulus of a piezoelectric patch shunted with only inductance, it is expressed as

$$E_p = E_p^{\text{sc}} \frac{\omega_{LC}^2 - \omega^2 / (1 - k_{31}^2)}{\omega_{LC}^2 - \omega^2}. \quad (\text{A.2})$$

Figure A2 shows the variation of E_p when the frequency changes. It can also be seen that a resonance occurs at f_0 , in other words, E_p has a pole at the resonance frequency of the shunt.

From the above results, one can conclude that, in a resonant piezoelectric metamaterial, the occurrence of a bandgap is associated with a pole of the equivalent Young's modulus of the shunted patches (namely, E_p).

Appendix B. Numerical prediction of bandgaps

To predict the bandgaps obtained from the transfer function, a numerical method based on the Bloch wave expansion and finite element method are used. This numerical method is briefly introduced hereinafter, more details of this method can be found in [37].

The studied unit cell with shunted piezo-patches (PZT) in the numerical method is shown in figure B1. Ω_m and Ω_e indicate the domains of host structure and patches, respectively. S_t , S_b and S_l denote the top electrodes (connected to the shunts), bottom electrodes (grounded) and lateral surfaces of the patches, respectively.

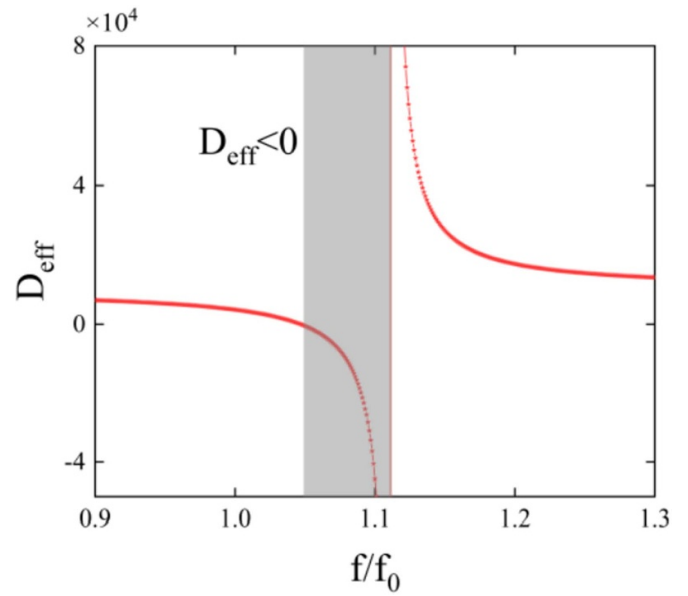


Figure A1. Variation of the equivalent bending stiffness of the unit cell when the frequency changes. Patches in the unit cell are shunted with only inductance and $f_0 = \omega_{LC} / 2\pi$.

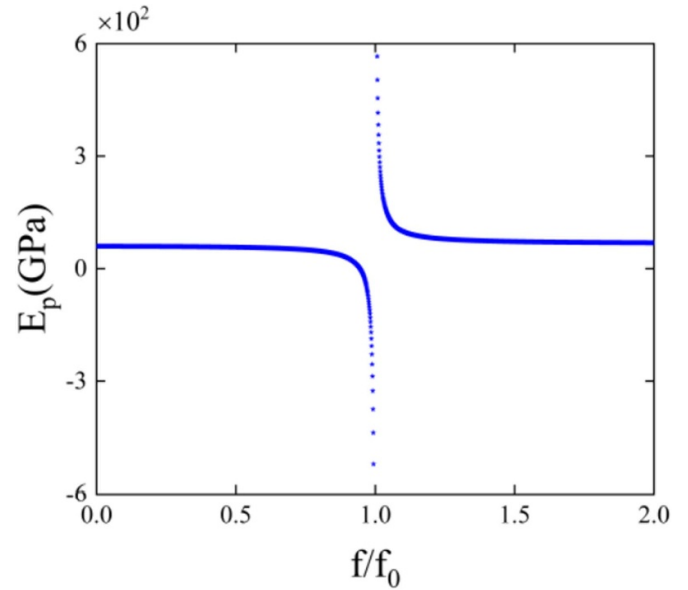


Figure A2. Variation of the equivalent Young's modulus of a piezoelectric patch shunted with a single inductance when the frequency changes, $f_0 = \omega_{LC} / 2\pi$.

The governing equations of the unit cell in time domain can be written as

$$\begin{aligned} \rho \ddot{\mathbf{w}}(\mathbf{x}, t) - \nabla \cdot \boldsymbol{\sigma}(\mathbf{x}, t) &= 0 \\ -\nabla \cdot \mathbf{D}(\mathbf{x}, t) &= 0 \end{aligned} \quad (\text{B.1})$$

in which, $\mathbf{w}(\mathbf{x}, t)$ is the displacement, \mathbf{D} is the electric displacement, ρ is the density, $\boldsymbol{\sigma}(\mathbf{x}, t)$ is the Cauchy stress tensor and $\boldsymbol{\sigma} = \mathbf{C} : \boldsymbol{\varepsilon}$, \mathbf{C} is the elasticity tensor, in the host structure, it is \mathbf{C}_m and in the patches it is \mathbf{C}_E , the Green strain tensor is $\boldsymbol{\varepsilon} = \nabla_{\text{sym}} \mathbf{w} = 1/2 (\nabla \mathbf{w}^T + \mathbf{w} \nabla^T)$.

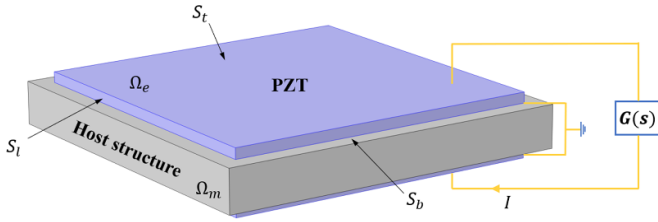


Figure B1. A representation of the studied unit cell.

The constitutive equations of piezoelectric materials can be written as:

$$\begin{aligned}\boldsymbol{\sigma} &= \mathbf{C}_E(\mathbf{x}) : \boldsymbol{\varepsilon} - \mathbf{e}^T(\mathbf{x}) \cdot \mathbf{E} \\ \mathbf{D} &= \mathbf{e}(\mathbf{x}) : \boldsymbol{\varepsilon} + \boldsymbol{\varepsilon}_s(\mathbf{x}) \cdot \mathbf{E}\end{aligned}\quad (\text{B.2})$$

in which, the electric field is $\mathbf{E} = -\nabla V$, \mathbf{e} is the coupling tensor, $\boldsymbol{\varepsilon}_s$ is the permittivity tensor under constant strain, $(\cdot)^T$ means transpose.

Based on equations (B.1) and (B.2), the governing equations of the unit cell are rewritten in frequency domain:

$$\begin{aligned}\rho\omega^2 \mathbf{w}(\mathbf{x}, \omega) + \nabla \cdot \mathbf{C} : \nabla_{\text{sym}} \mathbf{w}(\mathbf{x}, \omega) + \nabla \cdot \mathbf{e}^T \cdot \nabla V(\mathbf{x}, \omega) &= 0 \\ -\nabla \cdot \mathbf{e} : \nabla_{\text{sym}} \mathbf{w}(\mathbf{x}, \omega) + \nabla \cdot \boldsymbol{\varepsilon}_s \cdot \nabla V(\mathbf{x}, \omega) &= 0\end{aligned}\quad (\text{B.3})$$

and the electrical boundary conditions on each cell are as follows:

$$\begin{aligned}\mathbf{D} \cdot \mathbf{n} &= 0, \forall \mathbf{x} \in S_l \\ V &= 0, \forall \mathbf{x} \in S_b \\ V &= V^0, \forall \mathbf{x} \in S_t\end{aligned}\quad (\text{B.4})$$

in which V^0 is the voltage applied on the upper terminal of the patch. The relation between V^0 and the charges $q_0(t)$ (current is defined as $I = -\partial q_0(t)/\partial t$) fed into patches is

$$V^0(\omega) = -i\omega q_0(\omega) Z_{su}(\omega) \quad (\text{B.5})$$

Z_{su} is the impedance of the shunt.

The solution of equation (B.3) can be written as

$$\mathbf{u}(\mathbf{x}, \omega) = \begin{bmatrix} \mathbf{w} \\ V \end{bmatrix} = \mathbf{u}_{n,k} e^{i\mathbf{k} \cdot \mathbf{x}} \quad (\text{B.6})$$

$\mathbf{u}_{n,k} = \begin{bmatrix} \mathbf{w}_{n,k} \\ V_{n,k} \end{bmatrix}$ is the Bloch amplitude vector, it is composed of periodic functions, which means:

$$\begin{aligned}\mathbf{w}_{n,k}(\mathbf{x} - m\mathbf{P}) &= \mathbf{w}_{n,k}(\mathbf{x}) \\ V_{n,k}(\mathbf{x} - m\mathbf{P}) &= V_{n,k}(\mathbf{x})\end{aligned}\quad (\text{B.7})$$

here, $\mathbf{P} = [P_1 \ P_2]^T$ is the periodicity vector of the unit cell, m is an integer. This assumption imposes a mechanical boundary condition on the unit cell:

$$\begin{aligned}\mathbf{w}_{n,k}(\mathbf{x}_r) &= \mathbf{w}_{n,k}(\mathbf{x}_l) \\ \mathbf{w}_{n,k}(\mathbf{x}_t) &= \mathbf{w}_{n,k}(\mathbf{x}_b)\end{aligned}\quad (\text{B.8})$$

$\mathbf{x}_l, \mathbf{x}_r, \mathbf{x}_b, \mathbf{x}_t$ are positions on the left, right, bottom and top boundaries of the unit cell, respectively, as shown in figure B2.

Substituting equation (B.6) into equation (B.3) leading to

$$\begin{aligned}0 &= \rho\omega^2 \mathbf{w}_{n,k} + \nabla \cdot \mathbf{C} : \nabla_{\text{sym}} \mathbf{w}_{n,k} + \nabla \cdot \mathbf{e}^T \cdot \nabla V_{n,k} \\ &\quad + ik(\boldsymbol{\Theta} \cdot \mathbf{C} : \nabla_{\text{sym}} \mathbf{w}_{n,k} + \nabla \cdot \mathbf{C} : \Xi_{n,k}) \\ &\quad + ik(\nabla \cdot \mathbf{e}^T \cdot \boldsymbol{\Theta} V_{n,k} + \boldsymbol{\Theta} \cdot \mathbf{e}^T \cdot \nabla V_{n,k}) \\ &\quad - k^2(\boldsymbol{\Theta} \cdot \mathbf{C} : \Xi_{n,k} + \boldsymbol{\Theta} \cdot \mathbf{e}^T \cdot \boldsymbol{\Theta} V_{n,k}) \\ 0 &= -\nabla \cdot \mathbf{e} : \nabla_{\text{sym}} \mathbf{w}_{n,k} + \nabla \cdot \boldsymbol{\varepsilon}_s \cdot \nabla V_{n,k} \\ &\quad - ik(\boldsymbol{\Theta} \cdot \mathbf{e} : \nabla_{\text{sym}} \mathbf{w}_{n,k} + \nabla \cdot \mathbf{e} : \Xi_{n,k}) \\ &\quad + ik(\nabla \cdot \boldsymbol{\varepsilon}_s \cdot \boldsymbol{\Theta} V_{n,k} + \boldsymbol{\Theta} \cdot \boldsymbol{\varepsilon}_s \cdot \nabla V_{n,k}) \\ &\quad + k^2(\boldsymbol{\Theta} \cdot \mathbf{e} : \Xi_{n,k} - \boldsymbol{\Theta} \cdot \boldsymbol{\varepsilon}_s \cdot \boldsymbol{\Theta} V_{n,k})\end{aligned}\quad (\text{B.9})$$

in which, $\mathbf{k} = k[\cos(\theta) \ \sin(\theta) \ 0]^T = k\boldsymbol{\Theta}$, θ is the angle between wave vector \mathbf{k} and the x axis. $\Xi_{n,k}(\mathbf{x}) = 1/2(\mathbf{w}_{n,k} \boldsymbol{\Theta}^T + \boldsymbol{\Theta} \mathbf{w}_{n,k}^T)$ is a symmetric dyadic tensor.

In order to calculate the 2D dispersion curves, weak formulations are obtained by integrating Equation (B.9) projected onto any test function $\tilde{\mathbf{u}}_{n,k}$, they are expressed as

$$\begin{aligned}0 &= \int_{\Omega} \left[\rho\omega^2 \tilde{\mathbf{w}}_{n,k} \cdot \mathbf{w}_{n,k} - (\tilde{\boldsymbol{\varepsilon}}_{n,k} - ik\tilde{\Xi}_{n,k}) : \mathbf{C} : (\boldsymbol{\varepsilon}_{n,k} + ik\Xi_{n,k}) \right. \\ &\quad \left. - (\tilde{\boldsymbol{\varepsilon}}_{n,k} - ik\tilde{\Xi}_{n,k}) : \mathbf{e}^T \cdot (\nabla V_{n,k} + ik\boldsymbol{\Theta} V_{n,k}) \right] d\Omega \\ 0 &= \int_{\Omega} \left[(\nabla \tilde{V}_{n,k} - ik\boldsymbol{\Theta} \tilde{V}_{n,k}) \cdot \mathbf{e} : (\boldsymbol{\varepsilon}_{n,k} + ik\Xi_{n,k}) \right. \\ &\quad \left. - (\nabla \tilde{V}_{n,k} - ik\boldsymbol{\Theta} \tilde{V}_{n,k}) \cdot \boldsymbol{\varepsilon}_s \cdot (\nabla V_{n,k} + ik\boldsymbol{\Theta} V_{n,k}) \right] d\Omega \\ &\quad - \frac{\tilde{V}_{n,k}^0 V_{n,k}^0}{i\omega Z_{su}}\end{aligned}\quad (\text{B.10})$$

in which boundary conditions in equations (B.4), (B.5) and (B.8) are used.

Using the finite element method, equation (B.10) leading to an assembled matrix equation

$$[K(Z_{su}) - \omega^2 \mathbf{M} + \lambda(\omega, \theta) \mathbf{L} - \lambda^2(\omega, \theta) \mathbf{H}] \mathbf{u}(\omega, \theta) = 0 \quad (\text{B.11})$$

note that, the eigenvalue $\lambda = ik$, the eigenvector $\mathbf{u} = [w \ V]^T$ represents the Bloch amplitude, \mathbf{M} , \mathbf{H} and \mathbf{K} are symmetric, \mathbf{L} is skew-symmetric λ and \mathbf{u} can be solved when ω and θ are given.

The dispersion curves calculated by the aforementioned numerical method are shown in figure. A pole $\omega_0 = 2\pi f_0$ is assigned in the transfer function. Figures B3(a) and (b) show the real part and imaginary part of the wave number in frequency domain, respectively. The nonzero region of $\text{Im}(k)$ is corresponding to a bandgap.

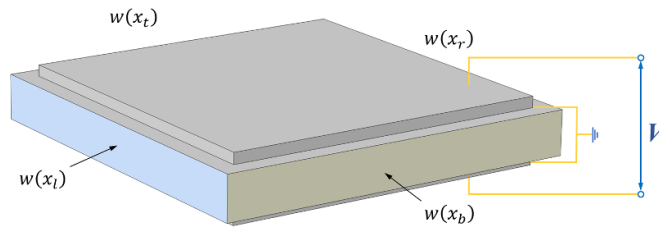


Figure B2. Boundary mechanical DOFs of the unit cell.

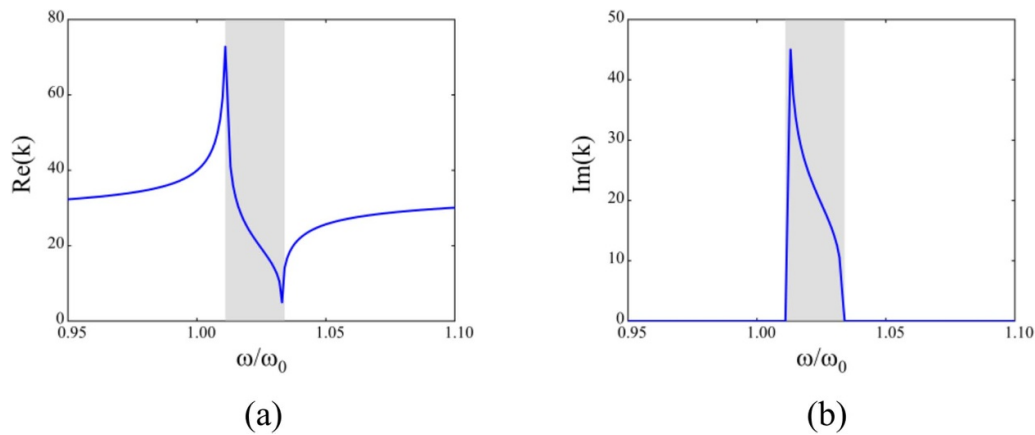


Figure B3. The dispersion curves calculated by the numerical method: (a) real part and (b) imaginary part. The shadowed areas indicate bandgap regions.

ORCID iDs

Kaijun Yi  <https://orcid.org/0000-0003-2215-5479>

Zhiyuan Liu  <https://orcid.org/0000-0002-3012-531X>

References

- [1] Liu Z, Sheng P, Zhang X X and Chan C T 2003 *Physica B* **338** 201–5
- [2] Yao S S, Zhou X M and Hu G K 2008 *New J. Phys.* **10** 043020
- [3] Huang G L and Sun C T 2010 *J. Vib. Acoustic.* **132** 031003
- [4] Tan K T, Huang H H and Sun C T 2012 *Appl. Phys. Lett.* **101** 241902
- [5] Tan K T, Huang H H and Sun C T 2014 *Int. J. Impact. Eng.* **64** 20–29
- [6] Li Q Q, He Z C, Eric L and Cheng A G 2019 *J. Appl. Phys.* **125** 035104
- [7] Zhu R, Huang G L and Hu G K 2012 *J. Vib. Acoustic.* **134** 031006
- [8] Barnhart Miles V, Xu X C, Chen Y Y, Zhang S, Song J Z and Huang G L 2019 *J. Sound Vib.* **438** 1–12
- [9] Hu G B, Tang L H, Das R, Gao S Q and Liu H P 2017 *AIP Adv.* **7** 025211
- [10] Hu G B, Tang L H and Das R 2018 *J. Appl. Phys.* **123** 055107
- [11] Pai P F, Peng H and Jiang S Y 2014 *Int. J. Mech. Sci.* **79** 195–205
- [12] Miranda J E J P, Nobrega E D, Ferreira A H R and Dos Santos J M C 2019 *Mech. Syst. Signal Process.* **116** 480–504
- [13] Tian Y J, Wu J H, Li H L, Gu C S, Yang Z R, Zhao Z T and Lu K 2019 *J. Phys. D: Appl. Phys.* **52** 395301
- [14] Gorshkov V, Sareh P, Navadeh N, Tereshchuk V and Fallah A 2021 *Mater. Design.* **202** 109522
- [15] Roca D, Cante J, Lloberas-Valls O, Pamies T and Oliver J 2021 *Extreme Mech. Lett.* **47** 101368
- [16] Forward R L 1979 *Appl. Opt.* **18** 690–7
- [17] Hagood N W and Von Flotow A 1991 *J. Sound Vib.* **146** 243–68
- [18] Thorp O, Ruzzene M and Baz A 2001 *Smart Mater. Struct.* **10** 979–89
- [19] Airolidi L and Ruzzene M 2011 *New J. Phys.* **13** 113010
- [20] Casadei F, Ruzzene M, Dozio L and Cunefare K A 2009 *Smart Mater. Struct.* **19** 015002
- [21] Casadei F, Delpero T, Bergamini A, Ermanni P and Ruzzene M 2012 *J. Appl. Phys.* **112** 064902
- [22] Chen S B, Wang G, Wen J H and Wen X S 2013 *J. Sound Vib.* **332** 1520–32
- [23] Sugino C, Ruzzene M and Erturk A 2020 *Int. J. Solids Struct.* **182** 281–94
- [24] Xiao X, He Z C, Eric L, Zhou B and Li X K 2020 *Compos. Struct.* **243** 112230
- [25] Wang G, Wang J W, Chen S B and Wen J H 2011 *Smart Mater. Struct.* **20** 125019
- [26] Wang G and Chen S B 2015 *Smart Mater. Struct.* **25** 015004
- [27] Cardella D, Celli P and Gonella S 2016 *Smart Mater. Struct.* **25** 085017
- [28] Li X P, Chen Y Y, Hu G K and Huang G L 2018 *Smart Mater. Struct.* **27** 045015
- [29] Airolidi L and Ruzzene M 2011 *J. Intell. Mater. Syst. Struct.* **22** 1567–79
- [30] Yi K J, Matten G, Ouisse M, Sadoulet-Reboul E, Collet M and Chevallier G 2020 *Smart Mater. Struct.* **29** 035005
- [31] Sugino C, Ruzzene M and Erturk A 2020 *Phys. Rev. Appl.* **13** 061001

- [32] Sugino C, Ruzzene M and Erturk A 2018 *IEEE/ASME Trans. Mechatron.* **23** 2144–55
- [33] Wang G, Cheng J Q, Chen J W and He Y Z 2017 *Smart Mater. Struct.* **26** 025031
- [34] Huang H H, Sun C T and Huang G L 2009 *Int. J. Eng. Sci.* **47** 610–7
- [35] Zhang H, Wen J H, Xiao Y, Wang G and Wen X S 2015 *J. Sound Vib.* **343** 104–20
- [36] Fleming A J, Behrens S and Moheimani S O R 2000 *Electron. Lett.* **36** 18
- [37] Collet M, Ouisse N and Ichchou M 2012 *J. Intell. Mater. Syst. Struct.* **23** 1661–77